coatings

MDPI

Article

Effect of Laser Remelting Energy Density on Microstructure and Properties of Laser Cladding IN 625 Layer

Mingyuan Li [1,2], Bocai Li [1,2], Zeqing Zhang [1,2], Xu Zhang [1,2], Desong Wang [1,2], Yinghuan Liu [1,2], Junmeng Wu [3,4] and Liang Zhang [2,3,4,*]

1 PowerChina Hebei Engineering Corporation Limited, Shijiazhuang 050021, China
2 Hebei Large-Scale Power Plant Turbine and Boiler Installation Technology Innovation Center, Shijiazhuang 050021, China
3 School of Materials Science and Engineering, Hebei University of Science and Technology, Shijiazhuang 050018, China
4 Hebei Key Laboratory of Material Near-Net Forming Technology, Hebei University of Science and Technology, Shijiazhuang 050018, China
* Correspondence: hebustzhangliang@163.com

Abstract

To enhance the comprehensive performance of laser cladding coatings, IN 625 alloy coatings were fabricated on Q345R steel substrates via laser cladding technology, followed by laser remelting treatment under varying laser energy densities. In this paper, the differences in microstructure and properties of the cladding layers without remelting and after laser remelting with different laser energy densities are studied. The experimental results show that laser remelting could effectively improve the surface roughness of the cladding layer. With the increase in laser energy density, the surface roughness initially decreased from 20.82 μm to 7.04 μm at 8 J/mm^2 and then increased to 10.28 μm at 12 J/mm^2. After laser remelting, the grain size of the cladding layer became more uniform, the number of equiaxed crystals increased, and the columnar crystals in the remelting area were broken to form short, rod-like columnar crystals. With the increase in laser energy density during remelting, the microhardness of the cladding layer gradually increased. The average microhardness of the cladding layer after remelting with 12 J/mm^2 laser energy density was about 265 $HV_{0.2}$, and the microhardness distribution was more uniform. With the increase in laser energy density, the corrosion resistance of the cladding-layer surface changed from an increase to a decrease. After remelting with a laser energy density of 8 J/mm^2, the cladding layer showed higher corrosion resistance, with the highest corrosion potential of −0.41 V and the minimum corrosion current density of 0.562 μA/cm^2.

Keywords: laser remelting; IN 625; laser energy density; microstructure; corrosion resistance

Check for updates

Academic Editor: Jaichan Lee

Received: 23 August 2026
Revised: 25 September 2026
Accepted: 28 September 2026
Published: 1 October 2026

Copyright: © 2026 by the authors. Licensee MDPI, Basel, Switzerland. This article is an open access article distributed under the terms and conditions of the Creative Commons Attribution (CC BY) license.

1. Introduction

Surface coatings are commonly used to protect industrial equipment and components against corrosion, wear, and related damage [1]. In recent years, the commonly used coating preparation technologies mainly include electroplating, spraying, surfacing, and cladding [2–7]. As an increasingly used coating technique, laser cladding provides concentrated heat input, low dilution, and strong metallurgical bonding, and has found applications in mechanical repair, chemical processing, energy, aerospace, and other fields [8–10]. Laser cladding is a process characterized by coupled interaction between the laser beam and

powder. The forming quality, microstructure, and mechanical properties of the cladding layer are generally governed by laser-related parameters (e.g., laser spot diameter, laser wavelength, laser type) as well as the thermophysical properties of cladding powders. Beyond these factors, key laser cladding process parameters, including laser power, scanning speed, powder feeding rate, and shielding gas flow rate, also exert dominant influences on the geometry, microstructure, and performance of the resulting cladding layer.

In laser cladding, a concentrated laser beam melts the delivered metal powder and forms a metallurgically bonded layer on the substrate. However, laser cladding components may exhibit high residual stress, surface roughness, pores, cracks, and compositional heterogeneity. When adopted for high-temperature pressure vessels, they struggle to satisfy long-term service requirements and are prone to potential safety risks, including corrosion-induced material failure. To solve the above problems, the surface of the cladding layer can be treated by laser remelting technology, so as to eliminate surface defects, reduce residual stress, homogenize the structure and composition, and improve the performance of the cladding layer [11–13].

In order to improve the corrosion resistance of carbon steel, laser cladding technology is commonly used to apply a more corrosion-resistant coating to the surface of carbon steel. Owing to their superior corrosion resistance and favorable tribological properties, selected stainless steels, nickel-based alloys, and cobalt-based alloys are widely adopted as coating materials [14]. Among these materials, nickel-based alloys have superior corrosion resistance and wider application. IN 625 is a solid-solution strengthened Ni-based alloy with Mo and Nb as principal strengthening elements, and exhibits good endurance, fatigue, oxidation, and corrosion resistance below 650 °C [15,16].

At present, many scholars have studied the surface-modification effect of laser cladding or remelting. Ge et al. [17] examined IN 625 coatings under various scanning speeds; faster scanning yielded finer dendrites, larger uniform equiaxed regions, and improved corrosion resistance because the increased grain-boundary density supplies more sites for passive-film nucleation and suppresses corrosion. Poza et al. [18] carried out laser remelting treatment on IN 625 cold-sprayed coating. After remelting, a columnar dendritic microstructure appeared, and porosity decreased, which increased the elastic modulus of the coating. Rico et al. [19] carried out laser remelting treatment on the ZrO_2 (CaO) composite ceramic coating on the surface of carbon steel. The ceramic coating was well bonded to the matrix. After laser remelting, the coating had fine grains and a dense microstructure. Hodgir et al. integrated positively defocused laser remelting into the fabrication of SS316L by laser directed energy deposition. Compared with the as-deposited condition, optimized remelting reduced porosity by up to 83% and increased microhardness by up to 34%, with these maxima obtained under different processing conditions. This strategy also improved surface finish and decreased solute segregation [20]. Nie et al. combined directed energy deposition and interlayer remelting to produce NiTi coatings. Their work examined grain refinement as a route to improved sliding wear resistance, demonstrating the value of incorporating remelting during deposition rather than limiting treatment to the final surface [21]. Jia et al. studied high-speed laser remelting of CoCrFeNiTi high-entropy alloy coatings deposited on copper substrates. Remelting removed unmelted regions and refined the coating microstructure. These changes improved hardness, wear resistance, and corrosion resistance, providing a surface-modification route for protecting copper substrates [22]. Li et al. used laser remelting on Fe-Cr-C-W coatings initially produced by arc cladding. Grain refinement and reduced porosity led to a 16% increase in microhardness. The remelted coating achieved a friction coefficient of 0.115 at 200 °C, indicating favorable frictional behavior under elevated-temperature testing [23]. Ding et al. used high-speed laser remelting to modify H13 coatings fabricated by ultra-high-speed laser cladding on

27SiMn steel. At a remelting power of 2200 W, surface roughness and wear loss decreased by 41.5% and 60.4%, respectively. Reduced elemental segregation and fewer cracks further improved coating integrity [24].

The coating structure and properties are closely linked to the laser-processing conditions. Many scholars have extensively examined how laser cladding parameters affect coatings and how laser remelting modifies different material surfaces, but there are few studies on the influence of laser remelting under different laser energy densities on the structure and properties of the coating. In this study, the IN 625 coating prepared by laser cladding technology was remelted using different laser energy densities. The surface morphology, microstructure, composition, hardness, and corrosion resistance of the coating before and after remelting were characterized and analyzed to further explore the influence of laser remelting energy density on the structure and performance of the remelted layer, which provides a theoretical basis for preparing laser cladding IN 625 coating with fine structure, uniform composition, and superior performance.

2. Experiment

2.1. Materials and Process

The substrates were Q345R carbon steel plates (HBIS Group Co., Ltd., Shijiazhuang, China) measuring 120 × 120 × 10 mm^3 with the chemical composition listed in Table 1. The IN 625 powder (Xi'an Sailong AM Technologies Co., Ltd., Xi'an, China) with a particle size of 100–200 μm was selected as the coating material, and its chemical composition is shown in Table 2. Before cladding, the substrates were ground to remove surface oxides and cleaned with anhydrous ethanol. The powder was vacuum-dried at 150 °C for 1 h.

Table 1. Chemical compositions of Q345R steel (wt%).

C	Mn	Si	S	P	Fe
0.20	1.56	0.55	0.008	0.03	Bal.

Table 2. Chemical composition of IN 625 powder (wt%).

Cr	Mo	Nb	Fe	Al	Ni
22.53	9.51	3.92	0.816	0.387	Bal.

The cladding experiment was carried out on a laser cladding system with a maximum laser output power of 6000 W, a wavelength of 1064 nm in continuous-wave (CW) mode, and a spot diameter of 2 mm. A schematic of the laser-cladding process is shown in Figure 1. IN 625 powder entered the melt pool at 21 g/min, while high-purity argon was supplied at 14 L/min for shielding. The selected power, scanning speed, and overlap rate were 1800 W, 35 mm/s, and 75%, respectively. Finally, a serpentine path was adopted to form a multipass cladding layer.

After the laser cladding was completed, laser remelting experiments were carried out on its surface with different laser energy densities. Equation (1) defines the areal energy density E from laser power P, spot diameter D, and scanning speed V. The remelting path was the same as the cladding path. The as-clad sample is denoted E0, and samples remelted at 4, 8, and 12 J/mm^2 are denoted E4, E8, and E12, respectively. The remelting parameters are shown in Table 3.

$$E = \frac{P}{D \times V} \quad (1)$$

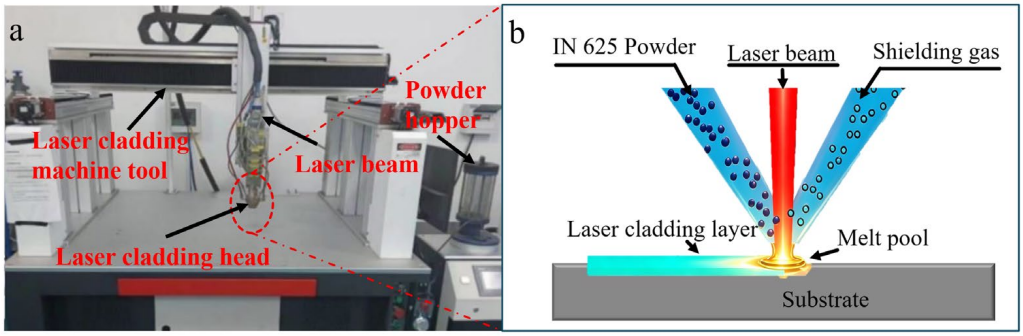


Figure 1. The schematic of the laser-cladding process: (**a**) laser cladding equipment; (**b**) schematic of the laser cladding process.

Table 3. Technological parameters of laser remelting.

	Laser Power (W)	Scan Speed (mm/s)	Laser Energy Density (J/mm^2)	Spot Diameter (mm)	Protective Gas Flow (L/min)	Overlap Rate (%)
1	400	50	4			
2	800	50	8	2	14	75
3	1200	50	12			

2.2. Characterization

The surface topography of samples before and after laser remelting was analyzed using LEXT laser confocal equipment (OLS5100, Olympus Corporation, Tokyo, Japan). For metallography, the coating was electrolytically etched for 7 s in 10 wt% oxalic acid at 3 V and examined with a LEICA-DMi8 optical microscope (Leica Microsystems, Wetzlar, Germany). A ZEISS MT scanning electron microscope (SEM) (ZEISS Microscopy, Oberkochen, Germany) equipped with an Oxford MX energy-dispersive X-ray spectroscopy (EDS) (Oxford Instruments NanoAnalysis, High Wycombe, UK) system was used to examine the microstructure and elemental distribution. The phase composition of the cladding layers was characterized by X-ray diffraction (XRD; Rigaku SmartLab, Cu target, Rigaku Corporation, Tokyo, Japan). The scanning rate was set at 1°/min, the step size was 0.05°, and the 2θ scanning range covered 30° to 100°. The microhardness of the specimen was measured with a hardness tester (HVS-1000Z, Laizhou Huayin Testing Instrument Co., Ltd., Laizhou, China) under a constant load of 200 g for a dwell time of 15 s along the depth direction from the top surface of the cladding layer to the carbon steel substrate. On each specimen, a regular rectangular indentation grid was laid across the cross-section, spanning the cladding layer, the bonding interface, and the substrate. A total of 120 indentations were performed for each sample, with a fixed horizontal indent spacing of 500 μm and vertical indent spacing of 100 μm to ensure dense and full coverage of the detection area. This regular grid distribution guarantees the accuracy and continuity of the interpolated cloud map and effectively reflects the real hardness fluctuations at different depths. All microhardness tests were repeated three times at each grid position to eliminate accidental errors. The final hardness values at each measuring point were averaged.

A 10 × 10 × 10 mm^3 specimen containing both the coating and substrate was prepared for electrochemical testing. Electrochemical impedance spectroscopy (EIS) and potentiodynamic polarization tests were conducted sequentially at ambient temperature in 3.5 wt% NaCl. Electrochemical testing employed a three-electrode configuration: a platinum plate served as the auxiliary electrode, a saturated calomel electrode as the reference electrode, and the sample surface as the working electrode. The electrical lead was soldered to the substrate, and epoxy resin masked the specimen to expose a 10 × 10 mm^2 coating area. Before

testing, the surface was sequentially ground, rinsed with deionized water, and dried. Prior to polarization and EIS tests, each sample was immersed in the test solution to stabilize the electrochemical system. The open-circuit potential (OCP) was monitored for a stabilization duration of 1800 s until the OCP fluctuation was lower than 5 mV/min, ensuring a stable initial electrochemical state. Potentiodynamic polarization was recorded from −1.5 to 1.0 V versus OCP at 1 mV/s. EIS was measured at OCP with a 5 mV sinusoidal perturbation over 10^5–10^{-2} Hz. To ensure the accuracy and reproducibility of the electrochemical data, two parallel repeated tests were performed for each group of samples. The obtained EIS spectra were quantitatively fitted and analyzed via the ZView software (version 3.1) using a reasonable equivalent circuit model, and the fitting errors were controlled within 5% to guarantee the reliability of the fitted electrochemical parameters.

3. Results and Discussion

3.1. Effect of Laser Remelting Energy Density on Surface Topography

Figure 2 presents three-dimensional surface topography and the corresponding roughness maps of IN 625 cladding layers under different laser remelting parameters. The panels in the top row display the macroscopic three-dimensional surface morphological features of the cladding layers, which intuitively reflect the surface flatness, undulation, and morphological defects such as protrusions and pits of coatings before and after laser remelting. The subgraphs in the bottom row correspond to the quantitative roughness maps of the same detection area, which visualize the continuous variation in surface elevation and roughness amplitude. The color gradient represents the relative surface height variation: warmer colors (red and yellow) indicate higher surface protrusion positions with larger local height values, while cooler colors (blue and green) represent lower surface depression positions with smaller height values. The uniform or discrete distribution of color regions directly reflects the uniformity of surface roughness and the distribution of surface micro-defects.

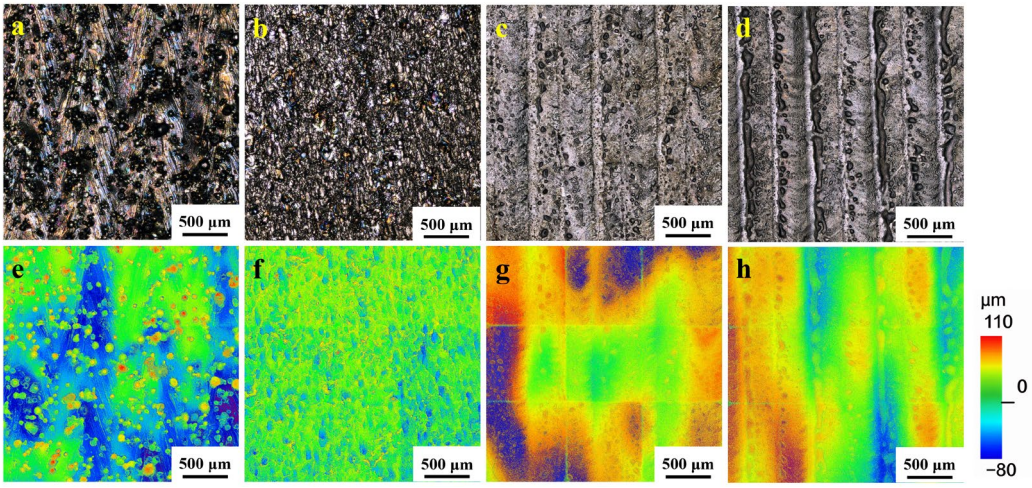


Figure 2. Surface topography of laser cladding IN 625: (**a**) Without remelting; (**b**) 4 J/mm^2; (**c**) 8 J/mm^2; (**d**) 12 J/mm^2; laser cladding IN 625 surface profile; (**e**) Without remelting; (**f**) 4 J/mm^2; (**g**) 8 J/mm^2; (**h**) 12 J/mm^2.

All surface roughness tests were conducted under consistent experimental conditions to ensure data reproducibility. The surface scanning area for each specimen was set to 3500 μm × 3500 μm. To eliminate experimental random errors and improve data reliability, three repeated measurements were randomly performed at different positions of each cladding-layer sample. The average roughness value (S_a) and corresponding standard deviation were calculated and recorded as the final experimental results, where the standard

deviation represents the experimental uncertainty of the roughness data. Remelting melted the residual surface powder and produced a smoother, flatter surface without visible pores or cracks.

The measured roughness values are summarized as follows. The non-remelted cladding layer has the highest mean roughness (S_a = 20.82 ± 0.68 μm) with pronounced undulation and nonuniform morphology. After laser remelting at 4 J/mm^2, Sa decreases to 13.59 ± 0.21 μm. At 8 J/mm^2, the surface becomes flatter, giving the lowest S_a (7.04 ± 0.43 μm) and the most uniform surface morphology. At 12 J/mm^2, however, excess heat accumulates on the coating surface. This surplus heat causes secondary remelting of the surface material, leading partially molten residual powder particles to aggregate and pile up locally. Such irregular agglomeration disrupts uniform surface morphology, producing micro-protrusions and uneven structures, and finally increases S_a to 10.28 ± 0.32 μm. Above 4 J/mm^2, greater melt-pool fluidity generally smooths the solidified surface; however, flow differences between the pool center and edge can leave a height gradient [25].

The distinct surface features observed in Figure 2 can be understood in terms of energy input and molten-pool dynamics. At too high an energy density, the pool agitates violently and metal vaporizes, ejecting droplets and causing heavy spatter, as seen in Figure 2a. At a moderate energy density, the pool remains stable, spatter is restrained, and the surface becomes relatively smooth (Figure 2b). Changing the parameters alters the heat input and overlap between neighboring tracks. Too little energy leaves the previous track only partially remelted, with residual pores and local protrusions at the overlaps (Figure 2c). Conversely, too much energy over-melts the track edges: strong Marangoni flow pushes molten metal to the crests, while deep grooves open up between adjacent passes (Figure 2d). A well-matched combination of energy density and overlap rate is therefore needed to suppress spatter, pores, and inter-track grooves, so that the clad coating reaches the desired surface quality.

3.2. Effect of Laser Remelting Energy Density on Microstructures

Figure 3 shows the microstructure of different regions of the cladding layer without laser remelting. The as-solidified morphology is governed by the ratio of temperature gradient G to growth rate R [26]. Near the bottom, heat escapes rapidly through the substrate, so G is high, and R is low, producing planar growth. Moving the front toward the surface, G drops while R rises, giving dendrites and columnar crystals. As grains grow opposite to the heat-flow direction, they extend roughly perpendicular to the coating/substrate interface [27]. At the top, cooling is so fast that nuclei form before they can grow, leaving mainly fine equiaxed crystals.

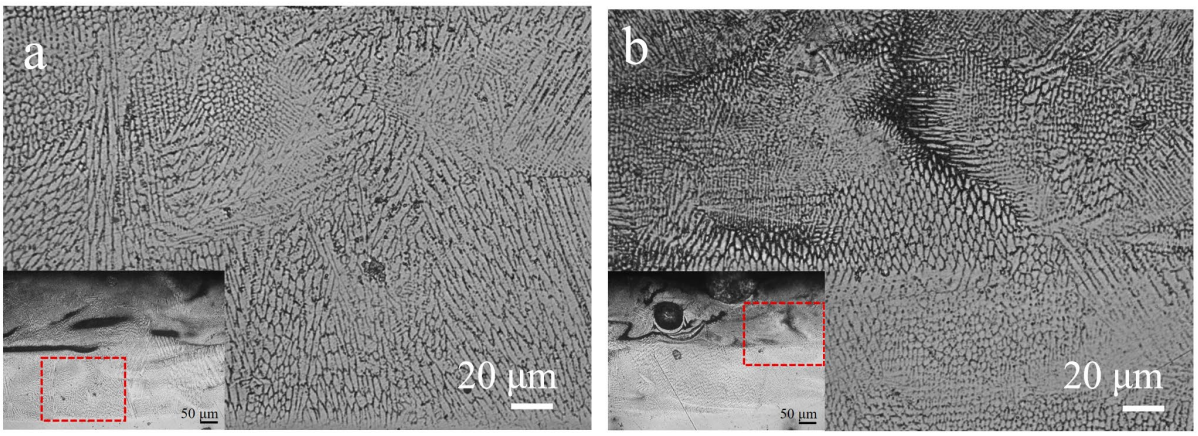


Figure 3. *Cont.*

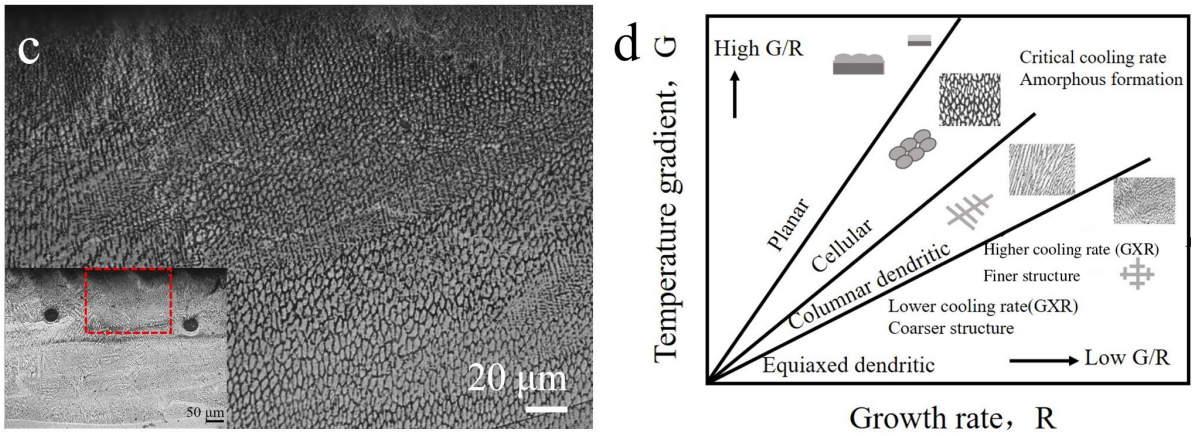


Figure 3. Microstructure of different regions of the cladding layer without remelting: (**a**) the bottom; (**b**) the middle; (**c**) the top; (**d**) Influence of temperature gradient (*G*) and growth rate (*R*) on transformation of solidification tissue morphology. The insets in panels (**a**–**c**) show lower-magnification views, with the red dashed boxes indicating the regions shown at higher magnification in the corresponding main images. Panel (**d**) schematically illustrates the relationship between the temperature gradient (G), growth rate (*R*), and solidification microstructure.

Figure 4 shows the microstructure of cladding layers at different positions before and after remelting. It can be seen from Figure 4a–d that the grains at the top of the cladding layer after laser remelting are mainly fine equiaxed crystals, and fine columnar crystals appear near the surface. Compared with the as-deposited condition, the remelted layer exhibits finer grains and a wider range of solidification morphologies, with both features strongly dependent on remelting energy density and the associated thermal field. In remelting, a highly concentrated energy pulse is delivered to the coating over an extremely short interaction time, imposing a rapid-heating and ultra-fast-cooling condition. Once the laser beam leaves the irradiated spot, the molten material solidifies without delay. Such a high cooling rate severely limits the time available for grain growth: heterogeneous nuclei form quickly while the newly formed grains have little chance to grow further, which is the essential reason why the remelted layer ends up with a fine and homogeneous microstructure. Distinct differences in surface morphology and solidification microstructure are observed under different laser energy density conditions. At a low laser energy density of 4 J/mm^2, the laser thermal input is relatively moderate, forming a large temperature gradient along the depth direction of the cladding layer during solidification. The directional heat dissipation dominates the solidification process, so the remelted cladding layer is mainly composed of elongated columnar crystals accompanied by a small number of fine equiaxed crystals. At this parameter, the remelting degree is sufficient to optimize the surface flatness of the original cladding layer, eliminate partial surface defects and uneven structures formed by primary cladding, and achieve a relatively dense and smooth surface morphology. Raising the energy density to 8 J/mm^2 broadens the molten pool and lowers the temperature gradient within it. As directional heat flow weakens, columnar crystals no longer grow preferentially. The pool then solidifies with a large number of fine equiaxed grains and short rod-like columnar crystals evenly distributed through the cladding layer. Relative to the 4 J/mm^2 case, the columnar aspect ratio drops markedly, and the whole microstructure becomes refined and homogeneous. At the same time, the more complete remelting removes the residual surface micro-pits and uneven ridges left by primary cladding, giving the best surface finish of all the tested groups. When the energy density climbs further to 12 J/mm^2, the surplus heat input produces pronounced heat accumulation within both the cladding layer and the substrate. The temperature gradient keeps falling, and the pool cools much more slowly. A longer high-temperature residence then

gives grains ample time to grow and rearrange. The fine nuclei formed earlier are able to grow fully, and some grains coarsen. The resulting microstructure consists mainly of coarse equiaxed grains and well-developed dendrites; oversized grains and uneven solidification shrinkage also slightly worsen the surface, raising the microscopic roughness. In addition to thermal field regulation, the laser thermal shock effect during remelting also plays a vital role in microstructure optimization. The high-energy laser beam acts on the original cladding layer, breaking the continuous and coarse columnar crystal structures formed in the primary cladding process. These fractured columnar crystal fragments remain in the molten pool and serve as new heterogeneous nucleation sites, significantly increasing the nucleation density of the molten material. Combined with the ultra-high cooling rate of laser remelting, newborn nuclei fail to obtain enough time for growth, thereby forming a large number of fine equiaxed grains. Nevertheless, the continuous increase in laser energy density changes the dominant mechanism of microstructure evolution: the grain growth effect induced by heat accumulation gradually overwhelms the grain refinement effect caused by rapid nucleation, which eventually leads to the transformation of the microstructure from fine short-columnar and equiaxed crystals to coarse equiaxed and dendritic crystals. In summary, the variation in laser remelting energy density regulates the temperature gradient, cooling rate, and thermal accumulation state of the molten pool, thereby dominating the surface morphology quality and solidification microstructure evolution of the remelted cladding layer [28,29].

Figure 4e–h shows the microstructure of the bottom part of the cladding layers without remelting and after remelting with different laser energy densities. In the bottom part of the cladding layer, the grain morphology is consistent with that before remelting, mainly columnar dendrites and cellular crystals. Under the thermal effect of laser remelting, more black particles precipitated at the grain boundary. With the increase in laser energy density, the thermal effect on the cladding layer interface increases, and the number of precipitates increases [30,31].

The top parts of the cladding layers without remelting and after remelting were photographed by scanning electron microscopy, and the results are shown in Figure 5. After laser remelting, the precipitates between grains are obviously reduced. At the top part of the cladding layer without remelting, there are a lot of Laves phases and carbides (MC and $M_{23}C_6$) between the grains. After remelting with a laser energy density of 4 J/mm^2, it can be seen that the Laves phases and the carbides between grains are significantly reduced. After remelting with a laser energy density of 8 J/mm^2, compared with the first two groups of experiments, Laves phases are significantly reduced, but compared with the cladding layer remelting with a laser energy density of 4 J/mm^2, its carbides are increased. When the laser energy density increases to 12 J/mm^2, the precipitates between grains are obviously reduced.

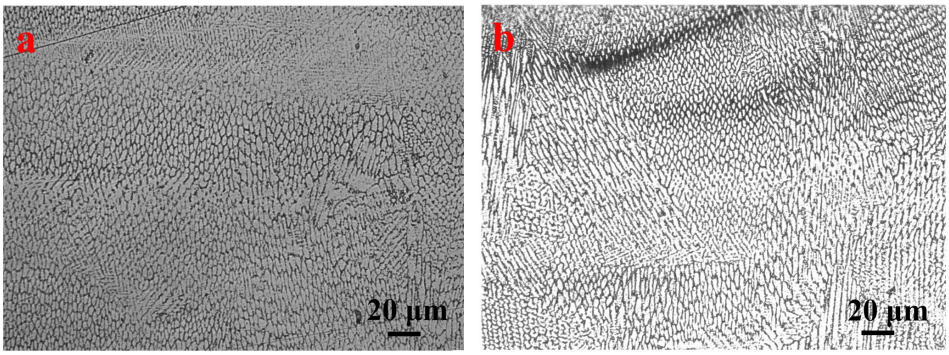


Figure 4. *Cont.*

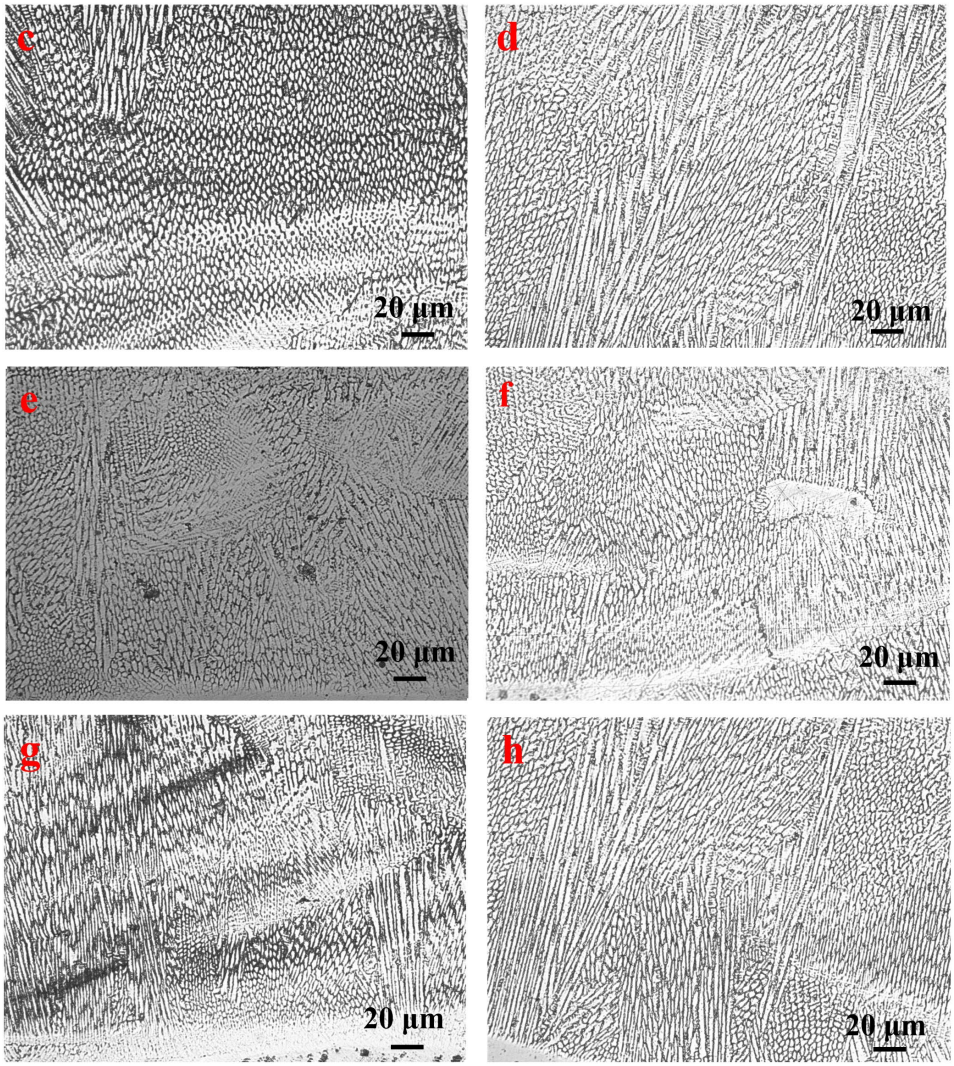


Figure 4. Microstructures of the top and bottom parts of the cladding layers without remelting and after remelting with different laser energy densities: (**a**) top part without remelting; (**b**) top part at 4 J/mm^2; (**c**) top part at 8 J/mm^2; (**d**) top part at 12 J/mm^2; (**e**) bottom part without remelting; (**f**) bottom part at 4 J/mm^2; (**g**) bottom part at 8 J/mm^2; (**h**) bottom part at 12 J/mm^2.

This is because elevated laser energy density enhances the flow of liquid metal within the molten pool, thereby accelerating the dissolution of the Laves phase. The as-prepared laser cladding layer exhibits severe segregation of Nb and Mo elements, which significantly degrades its high-temperature oxidation and corrosion resistance. Laser remelting treatment can substantially mitigate Nb and Mo segregation, suppress Laves-phase precipitation, and achieve more uniform grain size and compositional distribution within the remelted zone. EDS analysis performed on the top region of the remelted zone reveals that element distribution becomes more homogeneous after remelting relative to the non-remelted specimen. Meanwhile, increasing laser energy density further improves the compositional homogeneity of the cladding layer, as illustrated in Figure 6.

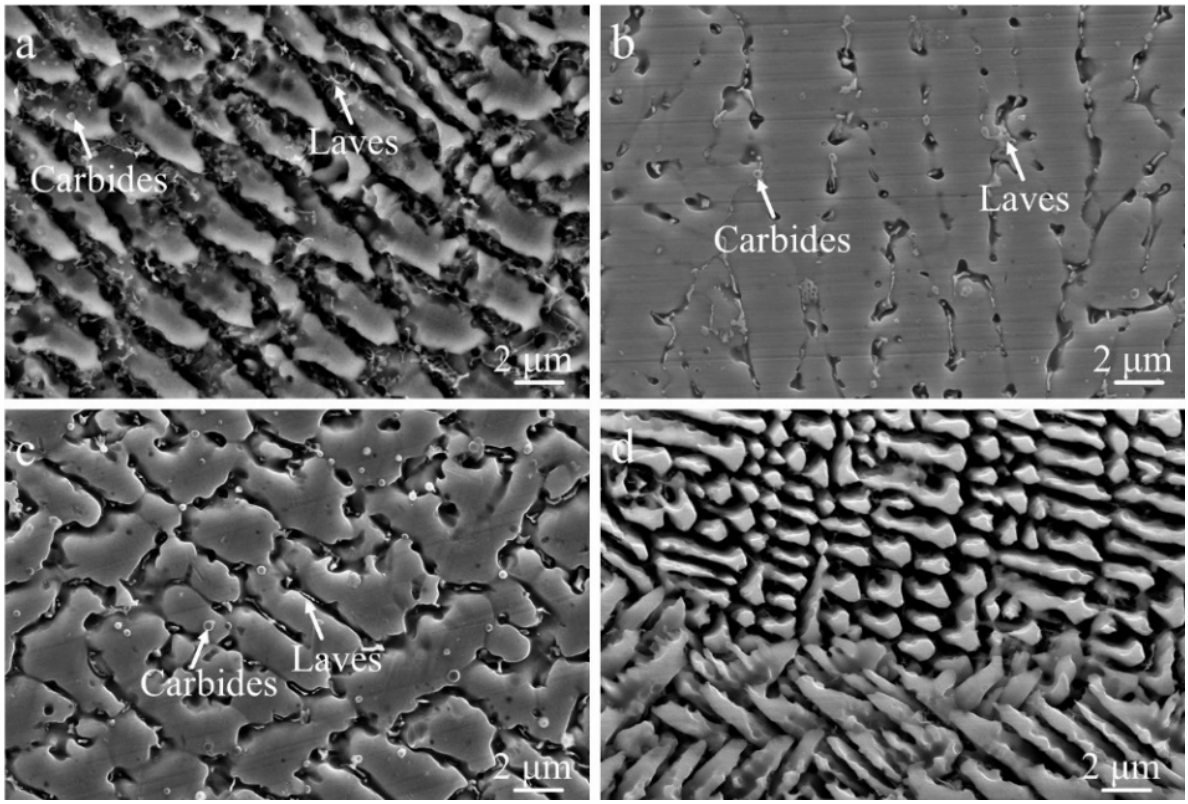


Figure 5. Microstructures of the top parts of the laser cladding layers without remelting and after remelting with different laser energy densities: (**a**) without remelting; (**b**) 4 J/mm^2; (**c**) 8 J/mm^2; (**d**) 12 J/mm^2.

Meanwhile, XRD tests were performed on the surface of the cladding layers to identify phase compositions under different laser-remelting energy densities, as shown in Figure 7. For the non-remelted sample, distinct diffraction peaks corresponding to the Laves phase and $M_{23}C_6$ carbides are clearly observed, together with intense diffraction signals of the γ matrix. This indicates that substantial Laves phases and $M_{23}C_6$ carbides exist in the as-deposited cladding layer, which is consistent with SEM observations showing abundant intergranular precipitates at the top region of the non-remelted cladding layer. At a laser-remelting energy density of 4 J/mm^2, the diffraction-peak intensities of the Laves phase and $M_{23}C_6$ carbides are markedly lower than those of the non-remelted sample. This demonstrates that laser remelting at this energy level suppresses the formation of intergranular precipitates, with both Laves-phase and carbide fractions significantly reduced. As the energy density increases to 8 J/mm^2, the diffraction-peak intensity of the Laves phase decreases further, which suggests an increased amount of precipitated carbides under this condition. Under laser remelting at 12 J/mm^2, the diffraction peaks of the Laves phase and $M_{23}C_6$ carbides are further attenuated, and only prominent diffraction peaks originating from the γ-matrix can be identified. This reveals that intergranular precipitates are largely eliminated at such a high energy density. Sufficient laser energy facilitates adequate melting and chemical homogenization, thereby effectively restraining the formation of Laves phases and carbides at grain boundaries.

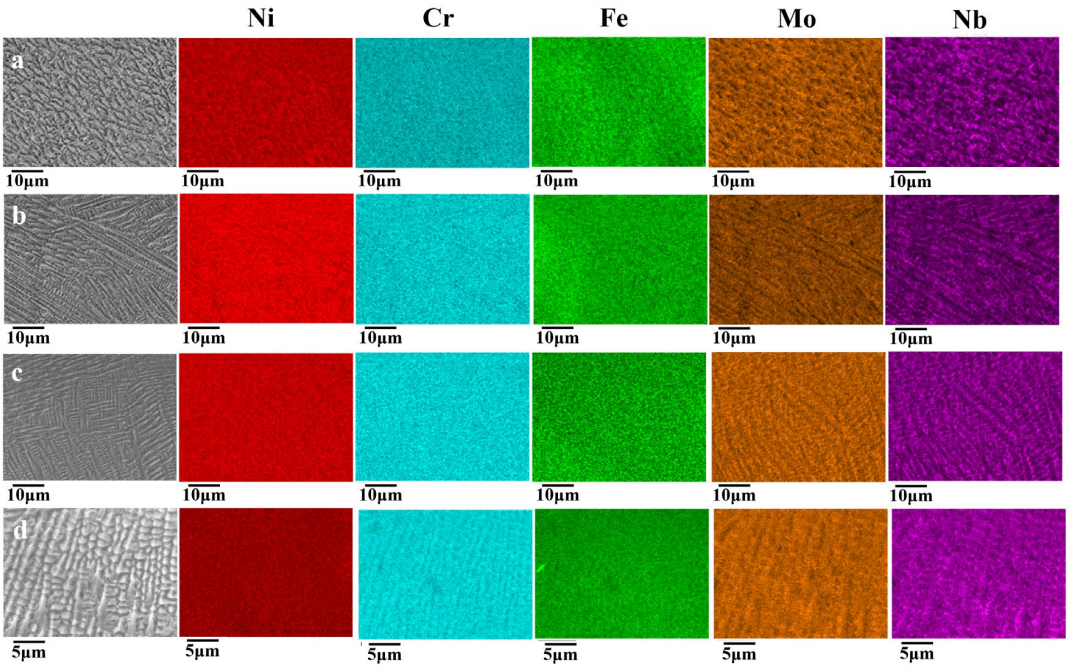


Figure 6. Element distribution of the top parts of the laser cladding layers without remelting and after remelting with different laser energy densities: (**a**) without remelting; (**b**) 4 J/mm^2; (**c**) 8 J/mm^2; (**d**) 12 J/mm^2.

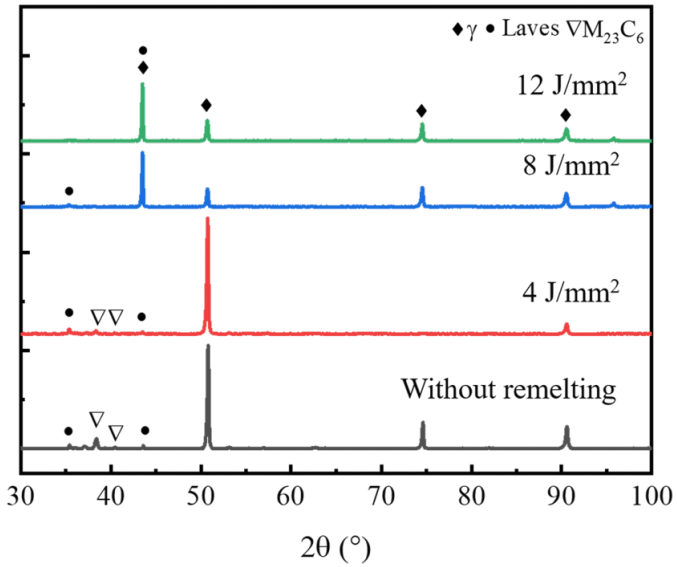


Figure 7. XRD patterns before laser remelting and after laser remelting with different energy densities.

3.3. Effect of Laser Remelting Energy Density on Microhardness

The microhardness distribution of the substrate and the cladding layers without remelting and after remelting with different laser energy densities was measured, and the cloud diagram was drawn. The results are shown in Figure 8. The test results indicate that all cladding layers exhibit distinctly higher microhardness than the substrate. Specifically, the average microhardness of the substrate is approximately 172 $HV_{0.2}$, while the average microhardness of the untreated as-clad layer reaches 252 $HV_{0.2}$. For the non-remelted cladding layer, the microhardness presents a gradual increasing trend from the top surface to the bonding interface with the substrate, with the surface microhardness measured at roughly 200 $HV_{0.2}$ and the interfacial microhardness up to 320 $HV_{0.2}$. The gradient hardness distribution at the cladding layer-substrate interface is presumably related to

carbon diffusion from the carbon-containing Q345R substrate toward the cladding layer during laser cladding. During rapid melting and solidification, carbon may migrate from the low-alloy substrate to the high-alloy cladding layer, which could promote carbide precipitation near the interfacial region. Apart from carbon migration, the interfacial hardness elevation may also originate from grain refinement induced by rapid solidification at the substrate-cladding boundary, as well as elemental interdiffusion between the coating and base metal.

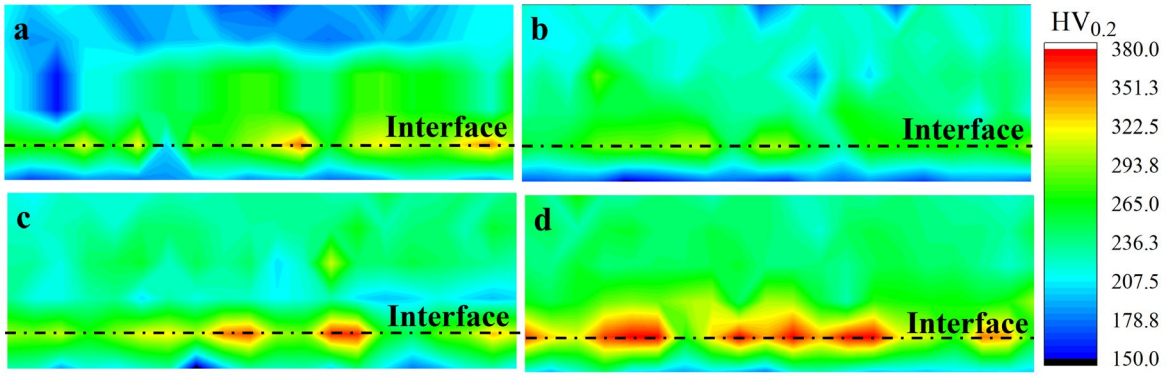


Figure 8. Hardness cloud diagram of the cladding layers without remelting and after remelting with different laser energy densities: (**a**) without remelting; (**b**) 4 J/mm^2; (**c**) 8 J/mm^2; (**d**) 12 J/mm^2.

Laser remelting further regulates the microhardness and hardness uniformity of the cladding layer. The microhardness of the remelted cladding layer increases progressively with the elevation of laser energy density. When the laser energy density rises to 12 J/mm^2, the average microhardness of the remelted cladding layer reaches 265 $HV_{0.2}$, which is higher than that of the non-remelted coating. In addition, increasing laser energy density effectively optimizes the hardness uniformity of the cladding layer and eliminates the excessive hardness gradient of the original coating. Two coupled strengthening mechanisms introduced by remelting account for this gain in hardness and uniformity. First, the rapid heating and ultra-fast cooling of remelting break down the coarse, uneven grains of the as-clad layer into a fine and homogeneous microstructure; the resulting grain-refinement strengthening removes the local hardness spikes caused by microstructural heterogeneity. Second, the higher energy density supplies enough heat to dissolve Nb, Mo, and other alloying elements fully into the matrix grains, strengthening the solid-solution effect. Acting together, grain refinement and solution strengthening raise both the average hardness and the uniformity of the remelted layer. In general, compared with the non-remelted cladding layer, laser remelting can effectively optimize the microhardness distribution, reduce the hardness difference, and improve the comprehensive mechanical performance of the coating, which fully verifies the excellent surface modification effect of laser remelting treatment.

3.4. Effect of Laser Remelting Energy Density on Corrosion Resistance

In the corrosion test, the potentiodynamic polarization curve test results are shown in Figure 9. In general, a more positive corrosion potential and a lower corrosion current density indicate better corrosion resistance [32]. Table 4 shows the electrochemical parameters of corrosion potential (E_{corr}) and corrosion current density (I_{corr}) obtained from the polarization curves by using the Tafel extrapolation method. It is found that the cladding layers after laser remelting have better corrosion resistance.

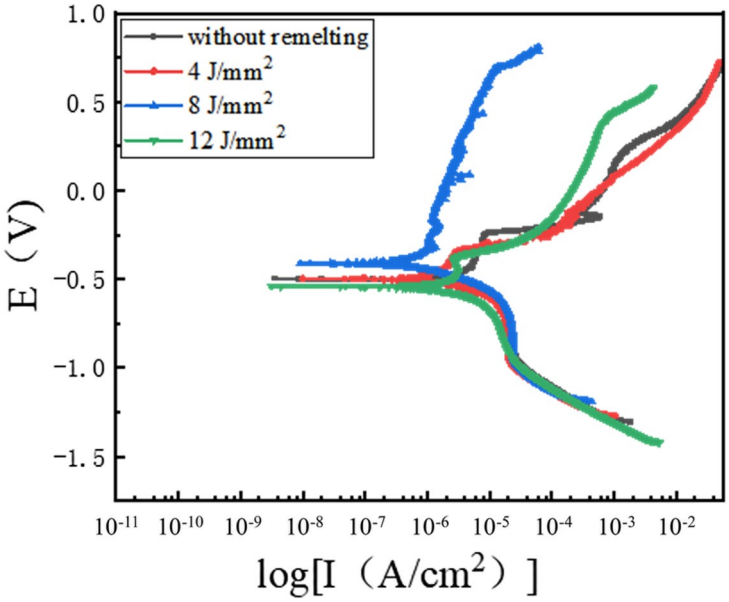


Figure 9. Test results of polarization curves of cladding layers without remelting and after remelting with different laser energy densities.

Table 4. Electrochemical parameters extracted from polarization curves in Figure 9.

	Without Remelting	4 J/mm^2	8 J/mm^2	12 J/mm^2
E_{corr} (V)	−0.51	−0.49	−0.41	−0.54
I_{corr} (μA/cm^2)	2.14	1.92	0.562	1.50

The highest corrosion potential (−0.41 V) and the lowest corrosion current density (0.562 μA/cm^2) of the cladding layer are obtained by remelting with the laser energy density of 8 J/mm^2, with the best corrosion resistance. In combination with the microstructure analysis, after remelting with a laser energy density of 8 J/mm^2, the cladding layer appears to have many fine columnar crystals and equiaxed crystals, and the fine grains and denser grain boundaries in the working area contribute to the improvement of corrosion resistance [33,34]. This is because the passive film prefers to nucleate at grain boundaries and twins; finer grains offer more such sites, and the film then spreads and joins into a compact layer [35]. A large number of Laves phases and carbides are distributed at grain boundaries in the upper region of the non-remelted cladding layer. After laser remelting, the intergranular precipitates are markedly reduced. At 4 J/mm^2, the amounts of intergranular Laves phases and carbides decrease remarkably. When the laser energy density increases to 8 J/mm^2, the fraction of Laves phases is further reduced compared with the former two groups, whereas more carbides are observed relative to the 4 J/mm^2 condition. As the laser energy density further rises to 12 J/mm^2, the intergranular precipitates decrease again, as shown in Figure 5. As the laser energy density increases from 4 to 8 J/mm^2, the dissolution and reduction in harmful Laves phases suppress local corrosion initiation. Meanwhile, grain refinement provides abundant high-energy grain boundaries for passive-film nucleation, promoting the formation of a compact passive film, which together contributes to the improved corrosion resistance. The dense passive film is easier to protect metals from corrosion by corrosive media. At the same time, carbides such as Cr and Nb distributed in the cladding layer can block the corrosion channel and inhibit the corrosion process [36,37].

The cladding layers without remelting and after remelting with different laser energy densities were subjected to EIS experiments in 3.5 wt% NaCl solution. The Nyquist

diagram (Figure 10a) and the Bode diagram (Figure 10b,c) were respectively drawn for the test results, and the equivalent circuit involved in the reaction in 3.5 wt% NaCl solution was analyzed. Figure 10d shows the equivalent circuit model when testing the impedance spectroscopy. Here, R_s, R_{ct}, and R_f denote the solution resistance, interfacial charge-transfer resistance, and passive film resistance, respectively. Q_f and C_{dl} represent the double electric layer between the solution–passive film interface and the passive film-electrode interface, respectively.

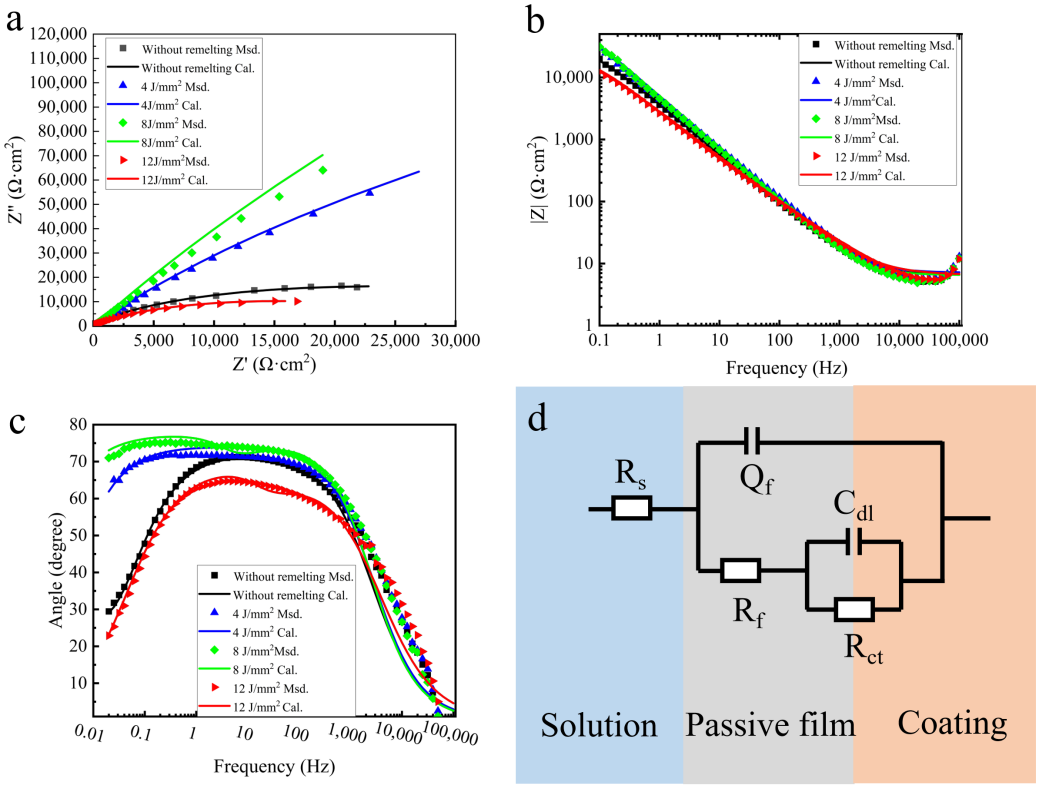


Figure 10. Test results of impedance spectrum curves of cladding layers without remelting and after remelting with different laser energy densities: (**a**) Nyquist plots; (**b**,**c**) Bode plots; (**d**) equivalent circuit model.

The diameter of the capacitive arc is a key indicator of corrosion resistance: a larger diameter corresponds to better corrosion resistance of the coating [38]. In the Nyquist diagram, the variation in semicircle diameter primarily reflects the difference in interfacial charge-transfer resistance, which determines the corrosion resistance of the coatings. The impedance modulus $|Z|$ and phase angle also matter: larger values indicate a more stable passive film and better corrosion resistance [39]. It can be observed from the EIS results that laser remelting treatment effectively improves the corrosion resistance of the cladding layer. However, further increasing the laser energy density to 12 J/mm^2 leads to a deterioration in the corrosion resistance of the remelted coating. According to the Nyquist diagram and Bode diagram, the cladding layer after remelting with the laser energy density of 8 J/mm^2 obviously has better corrosion resistance, which is consistent with the test results of the polarization curve. The resistance parameters are obtained by fitting and calculating the equivalent circuit, as shown in Table 5. The polarization resistance (R_p) of the sample in solution is the sum of R_s, R_f, and R_{ct}. The R_p of the cladding layer after remelting with the laser energy density of 8 J/mm^2 is the largest; thus, its corrosion resistance is the best.

After conducting electrochemical experiments in 3.5 wt% NaCl solution, phase analysis was carried out on the surface of the cladding layers without or after laser remelting. The

XRD test results are shown in Figure 11. The IN 625 cladding layer consists mainly of γ phase. After remelting with different laser energy densities, XRD experiments show that there are differences in the intensity of some diffraction peaks of the same phase. This phenomenon is mainly due to the grain rearrangement caused by multiple melting and crystallization after laser remelting [40]. During the polarization process, the following reactions occur on the IN 625 surface [41]:

$$Ni \rightarrow Ni^{2+} + 2\,e^{-} \quad (2)$$

$$Ni^{2+} + 2\,H_2O \leftrightarrow Ni(OH)_2 + 2\,H^{+} \quad (3)$$

$$Cr \rightarrow Cr^{3+} + 3\,e^{-} \quad (4)$$

$$Cr^{3+} + 3\,H_2O \leftrightarrow Cr(OH)_3 + 3\,H^{+} \quad (5)$$

$$Cr(OH)_3 + Cr \rightarrow Cr_2O_3 + 3\,H^{+} + 3\,e^{-} \quad (6)$$

$$Cr_2O_3 + 5\,H_2O \rightarrow 2\,CrO_4^{2-} + 10\,H^{+} + 6\,e^{-} \quad (7)$$

$$Ni^{2+} + CrO_4^{2-} \rightarrow NiCrO_4(s) \quad (8)$$

In the course of electrolytic corrosion, Ni and Cr dissolve anodically and first form loose $Ni(OH)_2$ and $Cr(OH)_3$ at the surface. As polarization continues, Cr_2O_3 develops and may further oxidize into soluble CrO_4^{2-}. After the test, $NiCrO_4$ is found abundantly on the surface. On the sample remelted at 8 J/mm^2, Cr_2O_3 is identified among the electrochemical corrosion products. The cladding layer remelted at 8 J/mm^2 exhibits higher reaction resistance, which suppresses electron-loss processes and retards subsequent corrosion. It is speculated that a relatively compact Cr_2O_3-rich oxide layer may remain on the surface, which potentially mitigates metal degradation induced by Cl^{-} attack [42]. Nevertheless, the available XRD and electrochemical data fail to provide direct evidence for the compactness and continuity of the formed oxide layer. As such, the proposed protective mechanism is still speculative and warrants further experimental validation.

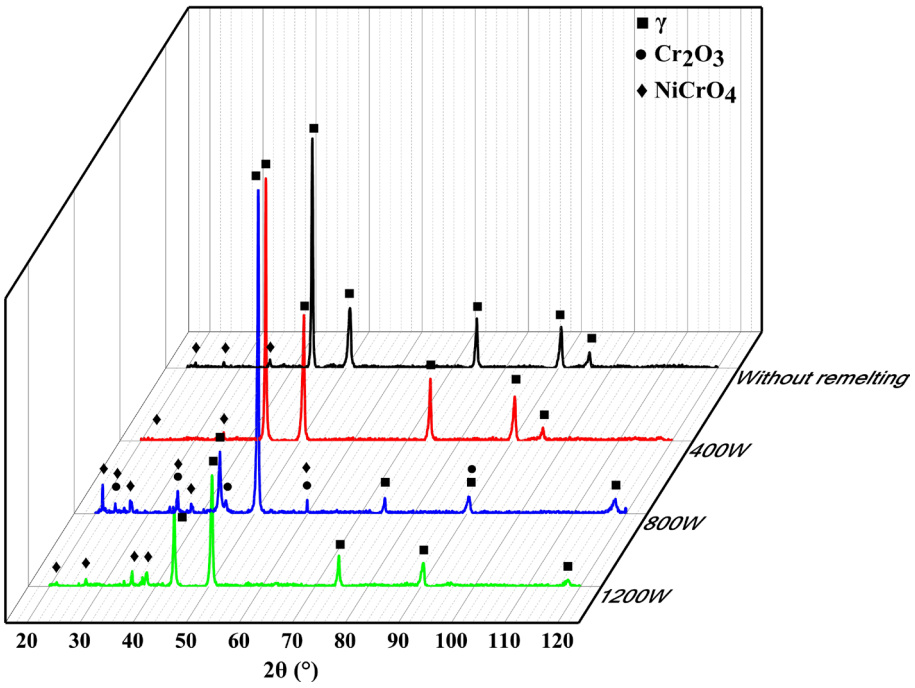


Figure 11. XRD patterns of each cladding layer after electrochemical corrosion.

Table 5. Fitting values of different resistances in the equivalent circuit.

	R_s ($\Omega \cdot cm^2$)	Q_f		R_f ($\Omega \cdot cm^2$)	C_{dl} (F)	R_{ct} ($\Omega \cdot cm^2$)
		CPE ($\Omega^{-1} \cdot cm^{-2} \cdot s^n$)	n			
Without remelting	6.559	6.13×10^{-5}	0.7748	4367	2.55×10^{-6}	5.14×10^4
4 J/mm^2	7.059	4.84×10^{-5}	0.7837	5750	1.88×10^{-6}	9.89×10^5
8 J/mm^2	6.497	4.09×10^{-5}	0.8461	7973	3.90×10^{-6}	1.83×10^6
12 J/mm^2	6.542	8.37×10^{-5}	0.7423	1841	4.84×10^{-6}	2.82×10^4

4. Conclusions

In this paper, an IN 625 coating was prepared on the surface of Q345R steel by using laser cladding technology, and the coating was remelted with different laser energy densities. The surface morphology, microstructure, hardness, and corrosion resistance of the coating without remelting and after remelting with different laser energy densities were compared and analyzed. The conclusions are as follows:

(1) Laser remelting effectively reduces the roughness of the IN 625 layer, which first decreases and then increases with rising energy density. The 8 J/mm^2 remelted surface is the smoothest, falling from 20.82 μm to 7.04 μm, while at 12 J/mm^2 it rises again to 10.28 μm.

(2) After laser remelting, more regular equiaxed crystals and more slender columnar crystals and columnar dendrites appear in the microstructure of the cladding layer compared with that without laser remelting. The cladding layer remelted with the laser energy density of 8 J/mm^2 appears to have short-rod columnar crystals. When the laser energy density increases to 12 J/mm^2, the grains tend to coarsen, resulting in equiaxed crystal growth. At the same time, laser remelting can effectively improve the phenomenon of element segregation in laser cladding. With the increase in laser energy density, the Laves phase in the cladding layer gradually decreases. When the remelting energy density reaches 12 J/mm^2, there are almost no precipitates in the remelting region.

(3) After laser remelting, the hardness distribution of the cladding layer becomes uniform. With the increase in laser energy density, the hardness value of the cladding layer increases, and the hardness value of the cladding layer after remelting with a laser energy density of 12 J/mm^2 reaches the maximum, with an average of 265 $HV_{0.2}$.

(4) The corrosion potential of the cladding layer after remelting with a laser energy density of 8 J/mm^2 is the highest, −0.41 V, and the corrosion current density is the lowest, 0.562 μA/cm^2, with the best corrosion resistance, and the same results were obtained in the EIS test. XRD test results show that the main corrosion products on the surface of the cladding layer are $NiCrO_4$ and Cr_2O_3.

Author Contributions: M.L.: Methodology, Experiments, Data curation, Writing—original draft and editing. B.L.: Experiments. Z.Z.: Experiments. X.Z.: Experiments. D.W.: Experiments, Validation. Y.L.: Validation. J.W.: Experiments, Validation. L.Z.: Writing—review and editing. All authors have read and agreed to the published version of the manuscript.

Funding: This research was funded by the Hebei Large-scale Power Plant Turbine & Boiler Installation Technology Innovation Center Incentive Special Fund Project, grant number 247790269H.

Institutional Review Board Statement: Not applicable.

Informed Consent Statement: Not applicable.

Data Availability Statement: The raw data supporting the conclusions of this article will be made available by the authors on request.

Conflicts of Interest: Author Mingyuan Li, Bocai Li, Zeqing Zhang, Xu Zhang, Desong Wang and Yinghuan Liu were employed by the company PowerChina Hebei Engineering Corporation Limited. All authors declare that the research was conducted in the absence of any commercial or financial relationships that could be construed as a potential conflict of interest.

References

1. Li, Y.L.; Song, P.; Wang, W.Q.; Lei, M.; Li, X.W. Microstructure and wear resistance of a Ni-WC composite coating on titanium grade 2 obtained by electroplating and electron beam remelting. *Mater. Charact.* **2020**, *170*, 110674. [CrossRef]
2. Arora, H.S.; Perumal, G.; Rani, M.; Grewal, H.S. Facile and green engineering approach for enhanced corrosion resistance of Ni-Cr-Al_2O_3 thermal spray coatings. *ACS Omega* **2020**, *5*, 24558–24566. [CrossRef]
3. Alidokht, S.; Vo, P.; Yue, S.; Chromik, R. Cold spray deposition of Ni and WC-reinforced Ni matrix composite coatings. *J. Therm. Spray Technol.* **2017**, *26*, 1908–1921. [CrossRef]
4. Shi, Z.P.; Wang, Z.B.; Wang, J.Q.; Qiao, H.N.; Xiong, T.Y.; Zheng, Y.G. Effect of Ni interlayer on cavitation erosion resistance of NiTi cladding by tungsten inert gas (TIG) surfacing process. *Acta Metall. Sin.* **2020**, *33*, 415–424. [CrossRef]
5. Li, X.; Zhang, C.H.; Zhang, S.; Wu, C.L.; Liu, Y.; Zhang, J.B.; Shahzad, M.B. Manufacturing of Ti_3SiC_2 lubricated Co-based alloy coatings using laser cladding technology. *Opt. Laser Technol.* **2019**, *114*, 209–215. [CrossRef]
6. Yuan, W.Y.; Li, R.F.; Chen, Z.H.; Gu, J.Y.; Tian, Y.T. A comparative study on microstructure and properties of traditional laser cladding and high-speed laser cladding of Ni45 alloy coatings. *Surf. Coat. Technol.* **2021**, *405*, 126582. [CrossRef]
7. Lou, L.Y.; Zhang, Y.; Jia, Y.J.; Li, Y.; Tian, H.F.; Cai, Y.J.; Li, C.X. High-speed laser cladded Ti-Cu-NiCoCrAlTaY burn resistant coating and its oxidation behavior. *Surf. Coat. Technol.* **2020**, *392*, 125697. [CrossRef]
8. Shen, F.M.; Tao, W.; Li, L.Q.; Zhou, Y.D.; Wang, W.; Wang, S.L. Effect of microstructure on the corrosion resistance of coatings by extreme high speed laser cladding. *Appl. Surf. Sci.* **2020**, *517*, 146085. [CrossRef]
9. Zhu, L.D.; Xue, P.S.; Lan, Q.; Meng, G.R.; Ren, Y.; Yang, Z.C.; Xu, P.H.; Liu, Z. Recent research and development status of laser cladding: A review. *Opt. Laser Technol.* **2021**, *138*, 106915. [CrossRef]
10. Zhai, L.L.; Ban, C.Y.; Zhang, J.W. Investigation on Laser Cladding Ni-Base Coating Assisted by electromagnetic field. *Opt. Laser Technol.* **2019**, *114*, 81–88. [CrossRef]
11. Li, Y.J.; Dong, S.Y.; Yan, S.X.; Liu, X.T.; Li, E.Z.; He, P.; Xu, B.S. Elimination of voids by laser remelting during laser cladding Ni based alloy on gray cast iron. *Opt. Laser Technol.* **2019**, *112*, 30–38. [CrossRef]
12. Chong, K.; Zou, Y.; Wu, D.T.; Tang, Y.W.; Zhang, Y.G. Pulsed laser remelting supersonic plasma sprayed Cr_3C_2-NiCr coatings for regulating microstructure, hardness and corrosion properties. *Surf. Coat. Technol.* **2021**, *418*, 127258. [CrossRef]
13. Koike, R.; Misawa, T.; Aoyama, T.; Kondo, M. Controlling metal structure with remelting process in direct energy deposition of Inconel 625. *CIRP Ann.* **2018**, *67*, 237–240. [CrossRef]
14. Panossian, Z.; Almeida, N.L.; Sousa, R.M.F.; Pimenta, G.S.; Marques, L.B.S. Corrosion of carbon steel pipes and tanks by concentrated sulfuric acid: A review. *Corros. Sci.* **2012**, *58*, 1–11. [CrossRef]
15. Xu, F.J.; Lv, Y.H.; Liu, Y.X.; Shu, F.Y.; He, P.; Xu, B.S. Microstructural Evolution and Mechanical Properties of Inconel 625 Alloy during Pulsed Plasma Arc Deposition Process. *J. Mater. Sci. Technol.* **2013**, *29*, 480–488. [CrossRef]
16. Ramkumar, K.D.; Abraham, W.S.; Viyash, V.; Arivazhagan, N.; Rabel, A.M. Investigations on the microstructure, tensile strength and high temperature corrosion behaviour of Inconel625 and Inconel718 dissimilar joints. *J. Manuf. Process.* **2017**, *25*, 306–322. [CrossRef]
17. Ge, T.; Chen, L.; Gu, P.F.; Ren, X.D.; Chen, X.M. Microstructure and corrosion resistance of TiC/Inconel 625 composite coatings by extreme high speed laser cladding. *Opt. Laser Technol.* **2022**, *150*, 107919. [CrossRef]
18. Poza, P.; Múnez, C.J.; Garrido-Maneiro, M.A.; Vezzù, S.; Rech, S.; Trentin, A. Mechanical properties of Inconel 625 cold-sprayed coatings after laser remelting. Depth sensing indentation analysis. *Surf. Coat. Technol.* **2014**, *243*, 51–57. [CrossRef]
19. Rico, A.; Sevillano, F.; Múnez, C.J.; López, M.D.; Utrilla, V.; Rodríguez, J.; Poza, P. Effect of laser remelting on the tribological performance of thermal barrier coatings. *J. Nanosci. Nanotechnol.* **2012**, *12*, 4984–4990. [CrossRef]
20. Hodgir, R.; Singh, R.; Mujumdar, S. Simultaneous enhancement of build rate and microstructure in SS316L additive manufacturing through in-situ laser remelting. *J. Manuf. Process.* **2025**, *133*, 865–878. [CrossRef]
21. Nie, M.H.; Jiang, P.F.; Li, X.R.; Zhu, D.D.; Yue, T.L.; Zhang, Z.H. Directed energy deposition combined with interlayer remelting for improving NiTi wear resistance by grain refinement. *Tribol. Int.* **2025**, *202*, 110300. [CrossRef]
22. Jia, H.Y.; Li, X.M.; Chen, W.J.; Jia, L.M.; Dong, Z.S.; Yan, Z.Q. Influence of laser remelting on the microstructures evolution and properties of CoCrFeNiTi high-entropy alloy coatings by high-speed laser melting on copper substrates. *Appl. Surf. Sci.* **2025**, *703*, 163414. [CrossRef]
23. Li, Y.C.; Liu, X.; Dong, H.; Wang, Y. Exploring the microstructure and wear-resistance of Fe-Cr-C-W arc cladding coatings by laser remelting. *Surf. Coat. Technol.* **2025**, *513*, 132492. [CrossRef]

24. Ding, Y.H.; Jing, X.S.; Sun, Y.K.; Wang, Y.S.; Gui, W.Y. Laser remelting as a surface modification strategy for wear resistance improvement in ultra-high-speed laser cladding fabricated H13 coatings. *Mater. Des.* **2026**, *261*, 115345. [CrossRef]
25. Yi, P.; Mostaghimi, J.; Pershin, L.; Xu, P.Y.; Zhan, X.H.; Jia, D.L.; Yi, H.; Li, Y.C. Effects of laser surface remelting on the molten salt corrosion resistance of yttria-stabilized zirconia coatings. *Ceram. Int.* **2018**, *44*, 22645–22655. [CrossRef]
26. Duan, X.X.; Gao, S.Y.; Dong, Q.; Zhou, Y.F.; Xi, M.Z.; Xian, X.P.; Wang, B. Reinforcement mechanism and wear resistance of Al_2O_3/Fe-Cr-Mo steel composite coating produced by laser cladding. *Surf. Coat. Technol.* **2016**, *291*, 230–238. [CrossRef]
27. Yang, D.; Ning, Y.H.; Zhao, Y.G.; Zhu, G.; Xu, G.F. Influence of processing parameter on the microstructure, wear-resistance and corrosion-resistance of laser cladding Ni-based alloy on the surface of 304 stainless steel. *Mater. Rev.* **2017**, *31*, 133–140. [CrossRef]
28. Zhang, T.; Fan, Q.; Ma, X.L.; Wang, W.; Wang, K.S.; Shen, P.Q.; Yang, J.L.; Wang, L.Q. Effect of laser remelting on microstructural evolution and mechanical properties of Ti-35Nb-2Ta-3Zr alloy. *Mater. Lett.* **2019**, *253*, 310–313. [CrossRef]
29. Shin, G.H.; Choi, J.P.; Kim, K.T.; Kim, B.K.; Yu, J.H. Study on microstructures and hardness of STS316L fabricated by selective laser melting. *Korean Powder Metall. Mater. Inst.* **2017**, *24*, 210–215. [CrossRef]
30. Chikarakara, E.; Naher, S.; Brabazon, D. Spinodal decomposition in AISI 316L stainless steel via high-speed laser remelting. *Appl. Surf. Sci.* **2014**, *302*, 318–321. [CrossRef]
31. Brytan, Z.; Bonek, M.; Dobrzański, L.A.; Ugues, D.; Grande, M.A. The laser surface remelting of austenitic stainless steel. *Mater. Sci. Forum* **2010**, *654–656*, 2511–2514. [CrossRef]
32. Ziętala, M.; Durejko, T.; Polański, M. The microstructure, mechanical properties and corrosion resistance of 316L stainless steel fabricated using laser engineered net shaping. *Mater. Sci. Eng. A* **2016**, *677*, 1–10. [CrossRef]
33. Wu, Q.L.; Zhang, J.Q. Corrosion behavior of laser-clad Cu-9Ni-6Sn coating. *Surf. Coat. Technol.* **2018**, *349*, 1117–1129. [CrossRef]
34. Hu, L.W.; Liu, X.; Liang, C.H. Microstructure evolution and corrosion mechanism of laser cladded Zr-Cu-Ni-Al insitu metallic glass matrix composite coatings. *Surf. Coat. Technol.* **2021**, *409*, 126908. [CrossRef]
35. Chen, X.D.; Li, Y.S.; Zhu, Y.T.; Chen, Y.F.; Yang, B. Layer-by-layer corrosion behavior of 316LN stainless steel with a gradient-nanostructured surface. *Electrochem. Commun.* **2020**, *110*, 106642. [CrossRef]
36. Chen, L.; Sun, Y.Z.; Li, L.; Ren, X.D. Improvement of high temperature oxidation resistance of additively manufactured TiC/Inconel 625 nanocomposites by laser shock peening treatment. *Addit. Manuf.* **2020**, *34*, 101276. [CrossRef]
37. Sohrabi, M.J.; Mirzadeh, H.; Rafiei, M. Solidification behavior and Laves phase dissolution during homogenization heat treatment of Inconel 718 superalloy. *Vacuum* **2018**, *154*, 235–243. [CrossRef]
38. Sulima, I.; Kowalik, R.; Hyjek, P. The corrosion and mechanical properties of spark plasma sintered composites reinforced with titanium diboride. *J. Alloys Compd.* **2016**, *688*, 1195–1205. [CrossRef]
39. Liu, H.L.; Tong, Z.P.; Zhou, W.F.; Yang, Y. Improving electrochemical corrosion properties of AZ31 magnesium alloy via phosphate conversion with laser shock peening pretreatment. *J. Alloys Compd.* **2020**, *846*, 155837. [CrossRef]
40. Amanov, A. Effect of local treatment temperature of ultrasonic nanocrystalline surface modification on tribological behavior and corrosion resistance of stainless steel 316L produced by selective laser melting. *Surf. Coat. Technol.* **2020**, *398*, 126080. [CrossRef]
41. Schmuki, P.; Virtanen, S.; Davenport, A.J.; Vitus, C.M. Transpassive dissolution of Cr and sputter-deposited Cr oxides studied by in situ X-Ray near-edge spectroscopy. *J. Electrochem. Soc.* **1996**, *143*, 3997–4005. [CrossRef]
42. Jeyaprakash, N.; Yang, C.H.; Karuppasamy, S.S.; Dhineshkumar, S.R. Evaluation of microstructure, nanoindentation and corrosion behavior of laser cladded Stellite-6 alloy on Inconel-625 substrate. *Mater. Today Commun.* **2022**, *31*, 103370. [CrossRef]

Disclaimer/Publisher's Note: The statements, opinions and data contained in all publications are solely those of the individual author(s) and contributor(s) and not of MDPI and/or the editor(s). MDPI and/or the editor(s) disclaim responsibility for any injury to people or property resulting from any ideas, methods, instructions or products referred to in the content.